# High Resolution Doppler Imager observations of ozone in the mesosphere and lower thermosphere

Daniel R. Marsh
National Center for Atmospheric Research, Boulder, Colorado, USA

Wilbert R. Skinner, Alan R. Marshall, and Paul B. Hays
Department of Atmospheric, Oceanic, and Space Science, University of Michigan, Ann Arbor, Michigan, USA

David A. Ortland
Northwest Research Associates, Seattle, Washington, USA

Jeng-Hwa Yee
Applied Physics Laboratory, Johns Hopkins University, Laurel, Maryland, USA

Received 8 November 2001; revised 9 April 2002; accepted 10 April 2002; published 9 October 2002.

[1] Observations made by the High Resolution Doppler Imager (HRDI) onboard the Upper Atmosphere Research Satellite (UARS) of molecular oxygen Atmospheric band dayglow and temperature are used to infer ozone mixing ratios in the mesosphere and lower thermosphere. The retrieval relies on the fact that a significant portion of the dayglow originates from ozone photolysis. Observations cover up to 72° in latitude and an altitude range of 65–97 km, with a vertical resolution of 2.5 km. Error analysis shows that measurement errors in observed ozone volume mixing ratios are typically between 0.04 and 0.1 parts per million, although systematic errors may be larger. Measurements show good agreement with previous observations and with other UARS instruments. A unique feature of the HRDI mesospheric ozone data set is that all daylight local times are sampled, which allows resolution of large diurnal variations throughout the mesosphere. Dynamical signatures are clearly seen in the distribution of ozone, which indicates that vertical advection of atomic oxygen by the solar diurnal tide plays an important role in determining ozone concentrations. *INDEX TERMS:* 0340 Atmospheric Composition and Structure: Middle atmosphere—composition and chemistry; 0341 Atmospheric Composition and Structure: Middle atmosphere—constituent transport and chemistry (3334); 3384 Meteorology and Atmospheric Dynamics: Waves and tides; 3394 Meteorology and Atmospheric Dynamics: Instruments and techniques; *KEYWORDS:* mesospheric ozone, UARS, middle atmosphere, HRDI, airglow, diurnal tide

**Citation:** Marsh, D. R., W. R. Skinner, A. R. Marshall, P. B. Hays, D. A. Ortland, and J.-H. Yee, High Resolution Doppler Imager observations of ozone in the mesosphere and lower thermosphere, *J. Geophys. Res.*, *107*(D19), 4390, doi:10.1029/2001JD001505, 2002.

## 1. Introduction

[2] Observations of ozone in the mesosphere and lower thermosphere (MLT) are useful for several reasons. First, it is important that a baseline be established for ozone concentrations throughout the atmosphere, so that natural variability can be distinguished from anthropogenic perturbations. Second, ozone observations allow testing of atmospheric chemical models. Historically, modeling studies have often underpredicted ozone concentrations. One of the first comparisons between observed and modeled mesospheric ozone showed that a model based on accepted chemistry produced ozone up to 30% less than observations [*Solomon et al.*, 1983]. In the upper stratosphere the model deficit has been termed the "40 km problem" [see, e.g., *Siskind et al.*, 1995]. Recently, models have been brought into better agreement with observations in both the stratosphere and the mesosphere, but only after modifying key chemical kinetic rate constants [*Khosravi et al.*, 1998; *Mlynczak et al.*, 2000]. MLT ozone measurements can be used to test these modified chemical schemes by making model/data comparisons. Additionally, ozone is known to be an efficient absorber of ultraviolet radiation and reacts exothermically with several species including atomic hydrogen and oxygen [*Mlynczak and Solomon*, 1993]. Therefore, knowledge of ozone improves understanding of the energy balance in the MLT region. Finally, ozone concentrations are affected by atmospheric motions, and so ozone can be used as a tracer, allowing insight into MLT dynamics.

[3] The first satellite with an instrument specifically designed to make long-term observations of ozone in the upper mesosphere was the Solar Mesosphere Explorer (SME) satellite [*Thomas et al.*, 1984]. SME's Near Infrared Spectrometer measured the emission from $O_2(^1\Delta_g)$ at


0148-0227/02/2001JD001505

1.27 μm. The majority of $O_2(^1\Delta_g)$ is produced by the photolysis of ozone, and consequently it was possible to infer ozone from SME measurements of 1.27 μm emission. Observations were made in an altitude range of 50 to 90 km from December 1981 to December 1986. The nearly Sun-synchronous orbit of SME restricted observations to between 1500 and 1700 local time (LT). SME measurements confirmed the existence of the ozone secondary maximum first seen by *Hays and Roble* [1973] using stellar occultation.

[4] Satellite observations of mesospheric ozone continued with the launch of the Upper Atmosphere Research Satellite (UARS) on 12 September 1991 [*Reber et al.*, 1993]. UARS is comprised of 10 instruments, of which two were explicitly designed with the capability of making ozone measurements in the mesosphere. These instruments are the Microwave Limb Sounder (MLS) and the Halogen Occultation Experiment (HALOE).This paper presents a technique by which ozone measurements in the mesosphere can be made by a third instrument—the High Resolution Doppler Imager (HRDI). Sections 2 and 3 describe the instrument and the measurement technique. In section 4 error analysis is presented, followed by validation in section 5. Finally, section 6 will present HRDI observations that highlight the unique features of the HRDI data set.

## 2. HRDI Description

[5] The HRDI instrument is described in detail in the works *Hays et al.* [1993] and *Grassl et al.* [1995]. The instrument consists of a telescope, Fabry–Perot interferometer, and photosensitive detector. HRDI's primary purpose is to measure horizontal wind fields in the mesosphere and stratosphere. The HRDI telescope scans the atmosphere at azimuth angles of ±45° and ±135° relative to the orbit track. These viewing directions were chosen to allow sampling of the same volume from orthogonal directions and so allow estimates of the vector wind. The extent of the altitude scan depends on the operational mode. For example when measuring winds in the mesosphere, the altitude range is 50 to110 km. Typically the HRDI instrument will divide its observations equally between the mesosphere and the stratosphere, by switching observing modes either each orbit or each day. At an observation location, two scans are made; one up and one down. These scans take approximately one minute, in which time the satellite moves 4° along its orbital track. The horizontal resolution of observations therefore is about 500 km. The UARS satellite is in a near-circular orbit at an altitude of 585 km with an orbital inclination of 57°. This allows observations to range in latitude from either 73°N to 41°S or 41°N to 73°S, depending on which side of the satellite HRDI is observing.

[6] The HRDI instrument is capable of resolving individual rotational lines of atmospheric emissions in the spectral range between 557 and 776 nm. HRDI observes emission lines of the $O_2(b^1\Sigma_g \rightarrow X^3\Sigma_g)$ Atmospheric system. Centered at 762 nm, the *A* band (corresponding to the 0-0 vibrational transition) is the strongest band in the Atmospheric system and during the day the *A* band has an approximately constant volume emission rate of $10^5$ photons $cm^{-3}$ $s^{-1}$ between 60 and 95 km [*Wallace and Hunten*, 1968]. Mesospheric *A* band volume emission rates (VERs)

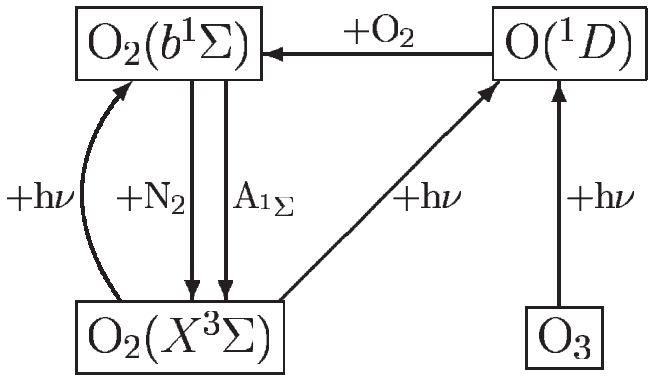


**Figure 1.** Schematic diagram showing processes relevant to Atmospheric band emission.

and temperatures have been determined by studying the brightness of rotational lines in the *A* band. Changes in a particular line's brightness are either due to a change in total band VER or a change in temperature. In order to determine whether a change in observed brightness results from a change in VER or T, observations of two lines with distinct temperature dependencies are compared. If both lines increase proportionately, then the change can be attributed to a change in VER. If the change is not proportionate then it can be inferred that there was a change in temperature. The fractional changes in temperature and VER from reference profiles are obtained from two nearly coincident limb scans made at differing wavelengths. An optimal estimate of these fractional changes is obtained by inverting a "forward" model that relates changes in brightness to changes in temperature and VER. The inversion technique used is described in detail by *Ortland et al.* [1998], and is based on the technique of *Rodgers* [1976]. Temperature profiles so obtained have been validated against a series of coincident rocket temperature soundings. Errors are estimated to be 7 K in recovered temperatures and 3% in the recovered VER.

## 3. Retrieval of Ozone Concentrations

[7] A method for the retrieval of ozone concentrations from *A* band VERs was first presented by *López-González et al.* [1992]. They derived an ozone profile from the only available *A* band dayglow observations at that time; those of *Wallace and Hunten* [1968]. The retrieval described here uses the same scheme, adapted for observations from the HRDI instrument, and incorporating recent laboratory measurements of absorption cross-sections and rate constants. A similar scheme has been used most recently by *Mlynczak et al.* [2001] to derive ozone concentrations from rocket observations of *A* band VER. The ozone derived from those observations was in good agreement with ozone derived from simultaneous measurements of $O_2(^1\Delta_g)$ emission.

[8] Retrieval of ozone concentrations relies on the fact that a significant portion of *A* band dayglow originates from ozone photolysis. A detailed discussion of the *A* band dayglow is presented by *Bucholtz et al.* [1986], and will only be summarized here. The two most significant sources of $O_2(b^1\Sigma_g)$ are resonance scattering and collisional excita-

**Table 1.** Reactions Relevant to the Chemistry of $O_2(b^1\Sigma_g)$

| Reaction | Symbol | Value[a] | Reference |
|---|---|---|---|
| $O_2(b^1\Sigma_g) \rightarrow O_2 + h\nu$ | $A_{1\Sigma}$ | 0.085 | *Burch and Gryvnak* [1969] |
| $O_2(b^1\Sigma_g) + N_2 \rightarrow$ products | $k_0$ | 2.1(−15) | *DeMore et al.* [1997] |
| $O_2(b^1\Sigma_g) + O_2 \rightarrow$ products | $k_4$ | 3.9(−17) | *DeMore et al.* [1997] |
| $O_2(b^1\Sigma_g) + O_3 \rightarrow$ products | $k_3$ | 2.2(−11) | *DeMore et al.* [1997] |
| $O_2 + h\nu \rightarrow O_2(b^1\Sigma_g)$ | $g$ | 5.56(−9) | see text |
| $O(^1D) + O_2 \rightarrow O + O_2$ | $k_1$ | 3.2(−11)exp(70/T) | *DeMore et al.* [1997] |
| $O(^1D) + O_2 \rightarrow O + O_2(b^1\Sigma_g)$ | $\phi k_1$ | $\phi$ = 0.95 (+0.05/−0.13) | *Green et al.* [2000] |
| $O(^1D) \rightarrow O + h\nu$ | $A_{1D}$ | 6.81(−3) | *Kernahan and Pang* [1975] |
| $O(^1D) + N_2 \rightarrow O + N_2$ | $k_2$ | 1.8(−11)exp(110/T) | *DeMore et al.* [1997] |
| $O_2 + h\nu \rightarrow O(^1D) + O$ | $J_2^*$ | | see text |
| $O_3 + h\nu \rightarrow O(^1D) + O_2^*$ | $J_3^*$ | | see text |
| $O + O + M \rightarrow O_2^* + M$ | $k_5$ | 4.7(−33)(300/T)$^2$ | *McDade et al.* [1986] |

[a] Second-order reaction rate constant units are cm$^3$ molecule$^{-1}$ s$^{-1}$. Read 2.1(−15) as $2.1 \times 10^{-15}$.

tion of molecular oxygen with $O(^1D)$ (shown schematically in Figure 1):

$$O_2(X^3\Sigma_g) + h\nu \rightarrow O_2(b^1\Sigma_g) \quad (1)$$

$$O(^1D) + O_2 \rightarrow O(^3P) + O_2(b^1\Sigma_g). \quad (2)$$

The rate of absorption for the $X^3\Sigma_g \rightarrow b^1\Sigma_g$ transition has been named the $g$-factor, and the rate of production of $O_2(b^1\Sigma_g)$ from this process is:

$$P_{res} = g[O_2], \quad (3)$$

where the notation [ ] refers to number density in molecules cm$^{-3}$. Similarly, the production rate of $O_2(b^1\Sigma_g)$ from collisional excitation with $O(^1D)$ can be written as,

$$P_{O(^1D)} = \phi k_1 [O(^1D)][O_2], \quad (4)$$

where $k_1$ is the quenching rate constant for $O(^1D)$ by $O_2$ and $\phi$ is the efficiency of this reaction for production of $O_2(b^1\Sigma_g)$. Values of $k_1$ and $\phi$ are listed in Table 1. along with other rate constants relevant to the chemistry of the Atmospheric bands.

[9] The only significant sources of $O(^1D)$ in the MLT are photolysis of ozone in the Hartley band and molecular oxygen in the Schumann–Runge continuum:

$$O_3 + h\nu(\lambda \leq 310\ nm) \rightarrow O(^1D) + O_2(^1\Delta_g) \quad (5)$$

$$O_2 + h\nu(\lambda \leq 176\ nm) \rightarrow O(^1D) + O(^3P) \quad (6)$$

The lifetime for $O(^1D)$ is very short (less than 0.001 s) throughout the MLT, because it is quickly de-excited by collisions with molecular oxygen and nitrogen. The concentration of $O(^1D)$ therefore depends on the photolysis rates of ozone and molecular oxygen, and on the quenching rate:

$$[O(^1D)] = \frac{J_3^*[O_3] + J_2^*[O_2]}{k_2[N_2] + k_1[O_2]}. \quad (7)$$

$J_3^*$ and $J_2^*$ are the photolysis rates for (5) and (6) respectively. In the MLT losses of $O(^1D)$ through spontaneous emission can be ignored since losses through quenching are larger than by a factor of at least a thousand.

[10] Figure 2 shows a simulated $A$ band VER between 60 and 115 km, derived from a background atmosphere based on the MSISE-90 empirical model of *Hedin* [1991], and ozone measurements from SME. Also shown are the individual contributions to the total VER from resonance scattering and the photolysis of ozone and molecular oxygen. Near 90 km these three processes are about equal sources of $O_2(b^1\Sigma_g)$. Above this altitude, molecular oxygen photolysis is the majority source, while below it is resonance scattering. The contribution from ozone photolysis ranges from 20% to 45% in the altitude range of 65 to 97.5 km, and thus allows inference of ozone concentrations.

[11] Figure 2 also shows a small contribution peaking near 95 km from a two-step Barth-type process:

$$\begin{aligned} O + O + M &\rightarrow O_2^* + M \\ O_2^* + O_2 &\rightarrow O_2(b^1\Sigma_g) + O_2, \end{aligned} \quad (8)$$

where $M$ is a "third body", i.e., molecular nitrogen or oxygen. The production of $O_2(b^1\Sigma)$ via this process can be estimated using a formulation based on the calculations of *McDade et al.* [1986],

$$P_{Barth} = k_5 \frac{[O]^2[O_2][M]}{C_{O_2}[O_2] + C_O[O]} \quad (9)$$

where the empirical constants $C_{O_2}$ and $C_O$ (equal to 7.5 and 33.0 respectively) are based on observations from seven rocket flights made during in March 1982.

[12] The Atmospheric band volume emission rate ($\eta$) for the $A$ band can now be considered as the emission resulting from the sum of three production terms for $O_2(b^1\Sigma_g)$:

$$\eta = F_c Q(P_{res} + P_{O(^1D)} + P_{Barth}). \quad (10)$$

$F_c$ is the Franck-Condon factor for the (0-0) transition (equal to 0.93 [*Nicholls*, 1965]), and $Q$ is the proportion of excited $O_2$ that actually emit a photon, instead of being quenched,

$$Q = \frac{A_{1\Sigma}}{A_{1\Sigma} + k_0[N_2] + k_4[O_2] + k_3[O_3]}, \quad (11)$$

where $A_{1\Sigma}$ is the Einstein coefficient for spontaneous emission. The denominator in (11) is dominated by

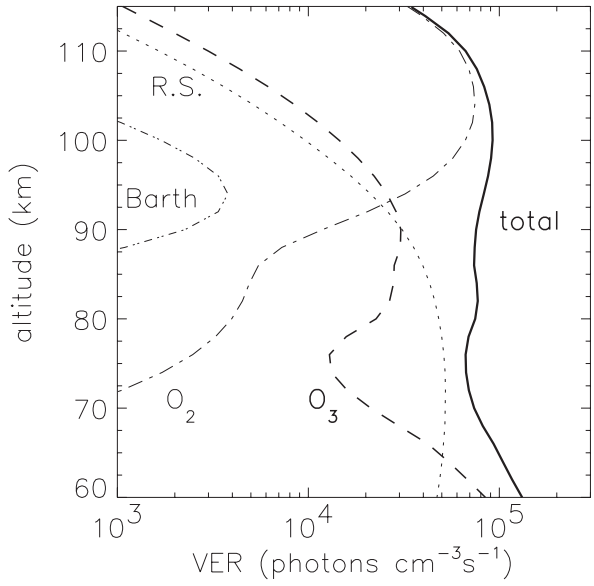


**Figure 2.** Simulated total A band VER (solid line) for 21 March 1993. Conditions are for overhead sun and moderate solar activity (F10.7 cm flux = 130). Also shown are contributions from ozone photolysis (dashed line), oxygen photolysis (dash-dotted line), resonance scattering (dotted line) and the Barth-type reaction (dash-triple dotted line).

spontaneous emission and quenching by $N_2$, which account for more than 95% of the losses. Substituting (7) into (10), leads to:

$$\eta = F_c Q \left( \frac{\phi k_1 \left( J_3^* [O_3] + J_2^* [O_2] \right)}{k_2 [N_2] + k_1 [O_2]} + g \right) [O_2] + F_c Q P_{Barth}. \quad (12)$$

[13] Retrieval begins by solving (12) for the concentration of ozone:

$$[O_3] = \left( \frac{\eta}{F_c Q [O_2]} - \frac{P_{Barth}}{[O_2]} - g \right) \times \left( \frac{k_2 [N_2] + k_1 [O_2]}{\phi k_1 J_3^*} \right) - \frac{J_2^*}{J_3^*} [O_2] \quad (13)$$

It is apparent from (13) that in order to calculate ozone, not only are measurements of $\eta$ required but also temperature since the reaction rate constants $k_1$ and $k_2$ are temperature dependent. The right-hand side of (13) is not independent of ozone, because ozone attenuates the solar flux used to calculate photolysis rates $J_2^*$ and $J_3^*$ However, photolysis rates can be calculated initially using a climatological ozone profile, and using (13) ozone concentrations can then be estimated. Calculation of the *g*-factor employs *k*-distribution theory [*Goody and Yung*, 1989]. The algorithms used were supplied by J.-H. Yee (personal communication, 1994) and have been shown to produce results consistent with previous calculations (R. DeMajistre and J.-H. Yee, A model for the rapid calculation of photon absorption (g factor) in the $O_2$ Atmospheric Bands, in preparation). An exo-atmospheric value of $5.56 \times 10^{-9}$ $s^{-1}$ is calculated. This is approximately 4% higher than the *Mlynczak* [1993] value, but this is to be expected, since the current method also includes the small contribution from the *B* band.

[14] The photolysis rates $J_2^*$ and $J_3^*$ are calculated over the spectral range from Lyman-$\alpha$ (121.6 nm) to 176 nm and 310 nm respectively. Solar fluxes are taken from the daily measurements of the Solar Ultraviolet Spectral Irradiance Monitor (SUSIM) [*Brueckner et al.*, 1993]. Molecular oxygen absorption cross-sections are from *Gibson et al.* [1983] (125–176 nm), *Koppers and Murtagh* [1996] (175–205 nm), and *Yoshino et al.* [1988] (185–242 nm). Ozone absorption cross-sections are from *Ackerman* [1971] ($\lambda <$ 185 nm), *Yoshino et al.* [1993] (185–245 nm), and *Molina and Molina* [1986] (245–345 nm). The quantum yields for $O(^1D)$ from ozone photolysis are approximately 90% throughout this spectral region. Values used to calculate $J_3^*$ are taken from the summary of *Cooper et al.* [1993] for wavelengths below 289 nm, from *Talukdar et al.* [1998] between 289 and 305 nm, and *DeMore et al.* [1997] above 305 nm. Quantum yields for $O(^1D)$ from molecular oxygen photolysis are unity below 176 nm and zero at longer wavelengths, except at Lyman-$\alpha$ where *Lacoursiere et al.* [1999], have determined a quantum yield of 0.53 ± 0.05.

[15] Ozone profiles are determined by using an iterative approach. Once an ozone profile is calculated, it is used to recalculate photolysis rates and the quenching factor, and a new estimate of ozone is retrieved. The process is repeated until there is no significant change in derived ozone profiles. Convergence is usually very fast with typically just two iterations required for profiles to agree to within 1%. In the process of calculating ozone profiles, $O(^1D)$ profiles are also calculated. This is a relatively simpler task, since the ozone and molecular oxygen photolysis rates are not needed in the retrieval (i.e., it is irrelevant which photolysis reaction produced $O(^1D)$). Therefore, it can be assumed that where there exists a HRDI ozone observation, a colocated $O(^1D)$ profile is also available.

## 4. Error Analysis

### 4.1. Measurement Error

[16] Measurement (or random) error in derived ozone results from measurement errors in observed input VER and temperature. Assuming that the errors in measured VER and temperature are uncorrelated, then the ozone variance ($\sigma^2_{O_3}$) can be calculated from (13) using the propagation of errors formula from the variances of the measured VER and temperature:

$$\sigma^2_{O_3} = \sigma^2_\eta \left( \frac{\partial [O_3]}{\partial \eta} \right)^2 + \sigma^2_T \left( \frac{\partial [O_3]}{\partial T} \right)^2$$

$$\sigma^2_{O_3} \simeq \sigma^2_\eta \left( \frac{k_2 [N_2] + k_1 [O_2]}{\phi k_1 J_3^* F_c Q [O_2]} \right)^2 + \sigma^2_T \left( \frac{40 k_2 [N_2]}{\phi J_3^* k_1 T^2} \right)^2 \cdot \left( \frac{\eta}{F_c Q [O_2]} - g \right)^2 \quad (14)$$

[17] Uncertainties in ozone resulting from uncertainties in model parameters such as reaction rates and photolysis rates are dealt with in the next section. Using (14), measurement errors are determined for each ozone profile. Figure 3b shows the average of all ozone measurement errors as a

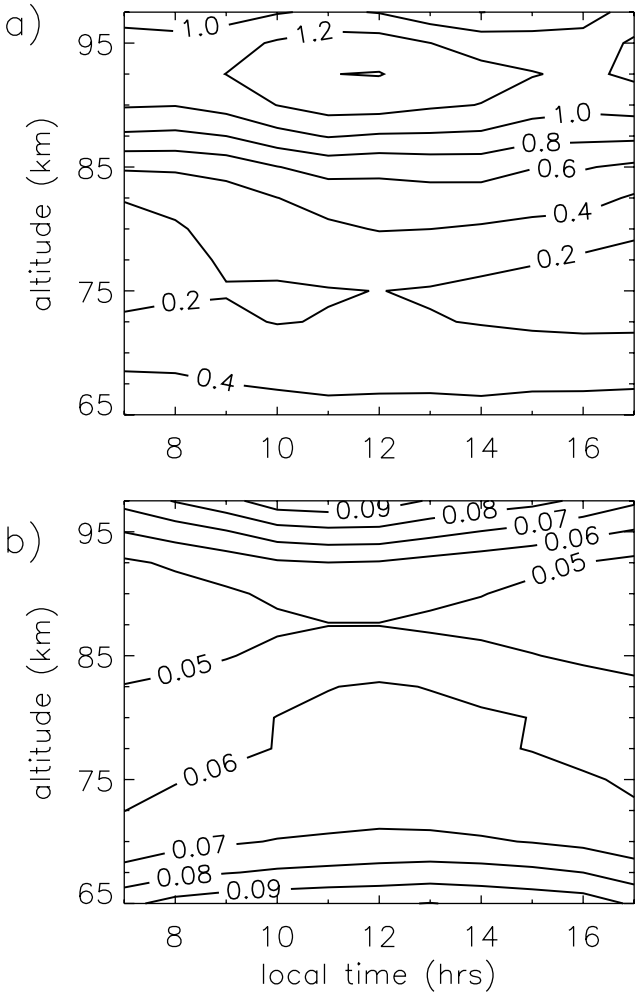


**Figure 3.** a) Hourly averaged ozone mixing ratios (ppmv) between 40°N and 40°S measured by HRDI during the period 22 April 1994 to 22 May 1994. b) Measurement errors (ppmv) in measured ozone in a) due to errors in VER and temperature.

function of local time for HRDI observations within 40° of the equator during April and May 1994. Errors fall in the range of 0.04 to 0.1 ppmv. Errors tend to be lowest near 90 km, where the relative contribution from ozone photolysis to the total VER is largest. Around 75 km, where very low ozone mixing ratios are observed near sunrise and sunset (see Figure 3a), this error is as large as 59% of the measured ozone. However, around the ozone secondary maximum at 92.5 km where measured ozone exceeds 1.4 ppmv, the error is as little as 4%.

### 4.2. Systematic Error

#### 4.2.1. Model Errors

[18] *Mlynczak and Olander* [1995] studied the effects of uncertainties in kinetic and spectroscopic rate constants in the retrieval of ozone concentrations from $O_2(b^1\Sigma_g)$ VER. Using uncertainties available at that time, they calculated systematic errors in the altitude range of 60 km to 97 km. Their calculations showed that the most significant sources of systematic error are uncertainties in $g$, $J_{O_3}$, $A_{1\Sigma}$, $\phi$, $k_0$, $k_1$, and $k_2$ (as defined in Table 1.), as well as $\Phi_{Ly-\alpha}$, the yield of $O(^1D)$ from $O_2$ photodissociation near Lyman-$\alpha$. The largest systematic errors (up to 809%) were due to the 30% uncertainty in $\phi$, the efficiency of production of $O_2(b^1\Sigma_g)$ from quenching by $O(^1D)$. A recent laboratory measurement has determined a value of 0.95 (+0.05/−0.13) [*Green et al.*, 2000] which more than halves the uncertainty from the previous measurement of *Lee and Slanger* [1978]. In addition, a new determination for the efficiency of production of $O(^1D)$ from molecular oxygen photolysis at Lyman-$\alpha$ has been made by *Lacoursiere et al.* [1999]. Following the approach of *Mlynczak and Olander* [1995], new systematic uncertainties have been calculated and are shown in Table 2. Table entries represent the percentage change in ozone after varying the model parameter by its uncertainty. Percentage changes are the differences in average ozone profiles for observations that fell within 20° of the equator on 21 March 1994 (a total of 128 profiles). Conditions are comparable to those of *Mlynczak and Olander* [1995], who chose a low latitude equinox conditions, and are generally for low solar zenith angles (maximum of 26°). The uncertainties in rate constants used to calculate these errors were as follows: 20% for $k_0$, $k_1$, and $k_2$; 5% for $A_{1\Sigma}$; 16% for $\phi$; and 15% for $g$. In general, new values for the systematic errors from the uncertainty in individual rate constants are much smaller (up to 68%). This reduction is in part due to improvements to measurement accuracies. Also, part of the difference may result from the previous estimate being based on a model atmosphere, and simulated VERs, whereas our estimates are based on observed VERs.

[19] Ozone concentration retrievals require knowledge of $N_2$ and $O_2$ number densities. These are obtained from the MSISE-90 empirical model. A sensitivity test was undertaken to determine the effect on the retrieval of a perturbation to the MSISE-90 background atmosphere. Relative changes in individual profiles of derived ozone with 10% increase in MSISE-90 $N_2$ and $O_2$ were calculated. Below 80 km the retrieval is relatively insensitive to the background atmosphere, with perturbed profiles being on average 1% larger. This can be understood by referring to (12) and

**Table 2.** Systematic Errors[a] in Retrieved Ozone Due to Errors in Rate Constants[b]

| Parameter: Uncertainty: | $g$ 15% | $J_{O_3}$ 15% | $A_{1\Sigma}$ 5% | $\phi$ 16% | $\Phi_{Ly}$ 9% | $k_2$ 20% | $k_1$ 20% | $k_0$ 20% |
|---|---|---|---|---|---|---|---|---|
| Altitude (km) | | | | | | | | |
| 97.5 | 9.2 | 14.3 | 3.5 | 37.2 | 1.8 | 39.4 | 32.7 | 18.0 |
| 95.0 | 8.1 | 14.2 | 3.1 | 24.5 | 1.6 | 25.7 | 21.4 | 16.8 |
| 92.5 | 7.5 | 14.1 | 3.0 | 18.3 | 1.5 | 19.2 | 15.9 | 16.9 |
| 90.0 | 8.5 | 14.2 | 3.2 | 16.0 | 1.6 | 16.7 | 13.8 | 19.3 |
| 87.5 | 13.4 | 14.7 | 3.6 | 15.4 | 2.4 | 15.9 | 13.2 | 25.7 |
| 85.0 | 24.7 | 15.6 | 4.1 | 15.5 | 4.0 | 16.1 | 13.4 | 39.4 |
| 82.5 | 30.3 | 15.8 | 4.4 | 15.6 | 4.2 | 16.1 | 13.4 | 48.7 |
| 80.0 | 24.9 | 15.0 | 4.6 | 15.1 | 2.9 | 15.7 | 13.0 | 45.7 |
| 77.5 | 29.2 | 14.8 | 4.7 | 15.0 | 2.6 | 15.5 | 12.9 | 53.0 |
| 75.0 | 37.0 | 14.5 | 4.8 | 14.9 | 2.2 | 15.4 | 12.8 | 64.3 |
| 72.5 | 38.7 | 14.0 | 4.8 | 14.6 | 1.4 | 15.1 | 12.5 | 68.0 |
| 70.0 | 29.7 | 13.5 | 4.8 | 14.4 | 0.5 | 14.8 | 12.3 | 57.7 |
| 67.5 | 21.4 | 13.3 | 4.8 | 14.3 | 0.1 | 14.7 | 12.2 | 47.5 |
| 65.0 | 15.3 | 13.3 | 4.8 | 14.3 | 0.0 | 14.7 | 12.2 | 40.0 |

[a] Systematic errors are in %.
[b] Parameter symbols refer to reactions listed in Table 1, except $\Phi_{Ly}$ (yield of $O(^1D)$ from $O_2$ photodissociation near Lyman-$\alpha$).

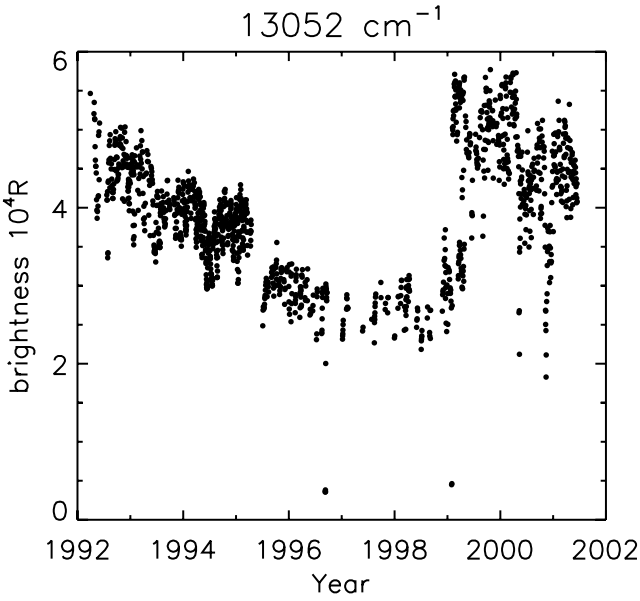


**Figure 4.** HRDI measured line of sight brightnesses at 13,052 cm$^{-1}$. Viewing tangent height is 87.5 km. Large scatter during November/December 2000 is due to loss of spacecraft attitude control.

considering only the predominant source of emission, i.e., resonance scattering and ozone photolysis.

$$\eta \propto \frac{A_{^1\Sigma}}{A_{^1\Sigma} + k_0[N_2]} \left( g + \phi k_1 J_3^* [O_3] \right) [O_2]. \quad (15)$$

Since, $k_0[N_2] \gg A_{^1\Sigma}$ and $[N_2] \propto [O_2]$ the emission rate becomes independent of density. As a result, calculated ozone densities are insensitive to model densities. Above 80 km the perturbed profiles are on average approximately 5% less than the unperturbed profiles. An increase in $O_2$ will lead to increased modeled production of $O(^1D)$ via $O_2$ photolysis. Less of the observed emission need originate through ozone photolysis to account for the observed emission rate. Therefore, above 80 km, ozone estimates will be lower for increased molecular oxygen concentrations.

#### 4.2.2. Instrument Sensitivity Accuracy

[20] Ozone retrievals require an accurate determination of VER and therefore spectral line intensities. This requires that the sensitivity of the HRDI instrument ($S$) be known, since it relates detector signal ($C$) to spectral brightness ($B$):

$$C = S \int I(\nu) B(\nu) d\nu, \quad (16)$$

where I is the normalized instrument function. Instrument sensitivity was measured in preflight calibration tests with an accuracy of approximately 10%. The VER and temperature are calculated from the ratios of lines in the $A$ band. Figure 4. shows average daily uncorrected line of sight brightnesses at 85 km tangent height for an individual emission line of the A band centered at 13,052 cm$^{-1}$. The long term downward trend in the brightness of approximately 8% per year is an instrumental effect, probably due to a loss of parallelism of the medium and low resolution etalons in the interferometer and resulting decrease in instrument sensitivity [*Skinner et al.*, 1999]. The trend is seen at all altitudes and at all wavelengths, and therefore is unlikely to be the result of a change in the atmosphere. An immediate increase in brightnesses is observed following a readjustment of the etalon calibration constants in 1999. Solar cycle effects would be altitude dependent and of a much smaller amplitude [*Keating et al.*, 1987]. Also, the brightness continued to decrease during the minimum of the solar cycle, when changes in solar ultraviolet flux were minimal.

[21] The observed trend in sensitivity must be corrected before ozone concentrations can be accurately retrieved. Since the HRDI instrument does not carry calibration light sources capable of measuring the throughput of the entire

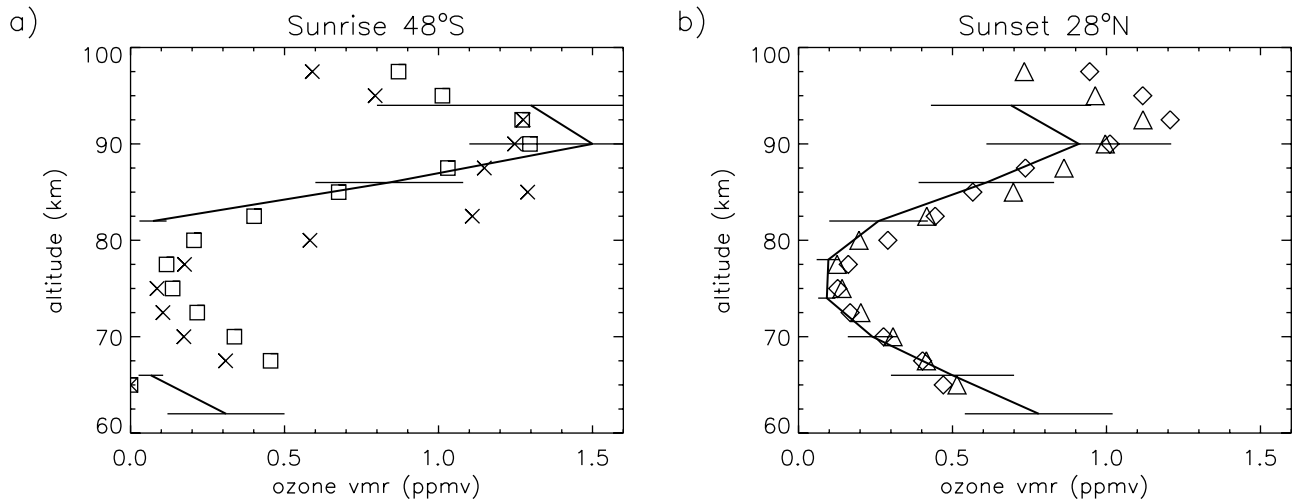


**Figure 5.** Comparison of ATMOS and HRDI ozone measurements. ATMOS data (solid line) are average of 2 sunrise profiles at 48°S, and 6 sunset profiles at 28°N. HRDI southern hemisphere data is from 26 April 1994 (crosses) and 28 April 1994 (squares). HRDI northern hemisphere data is from 30 April 1994 (triangles) and 2 May 1994 (diamonds).

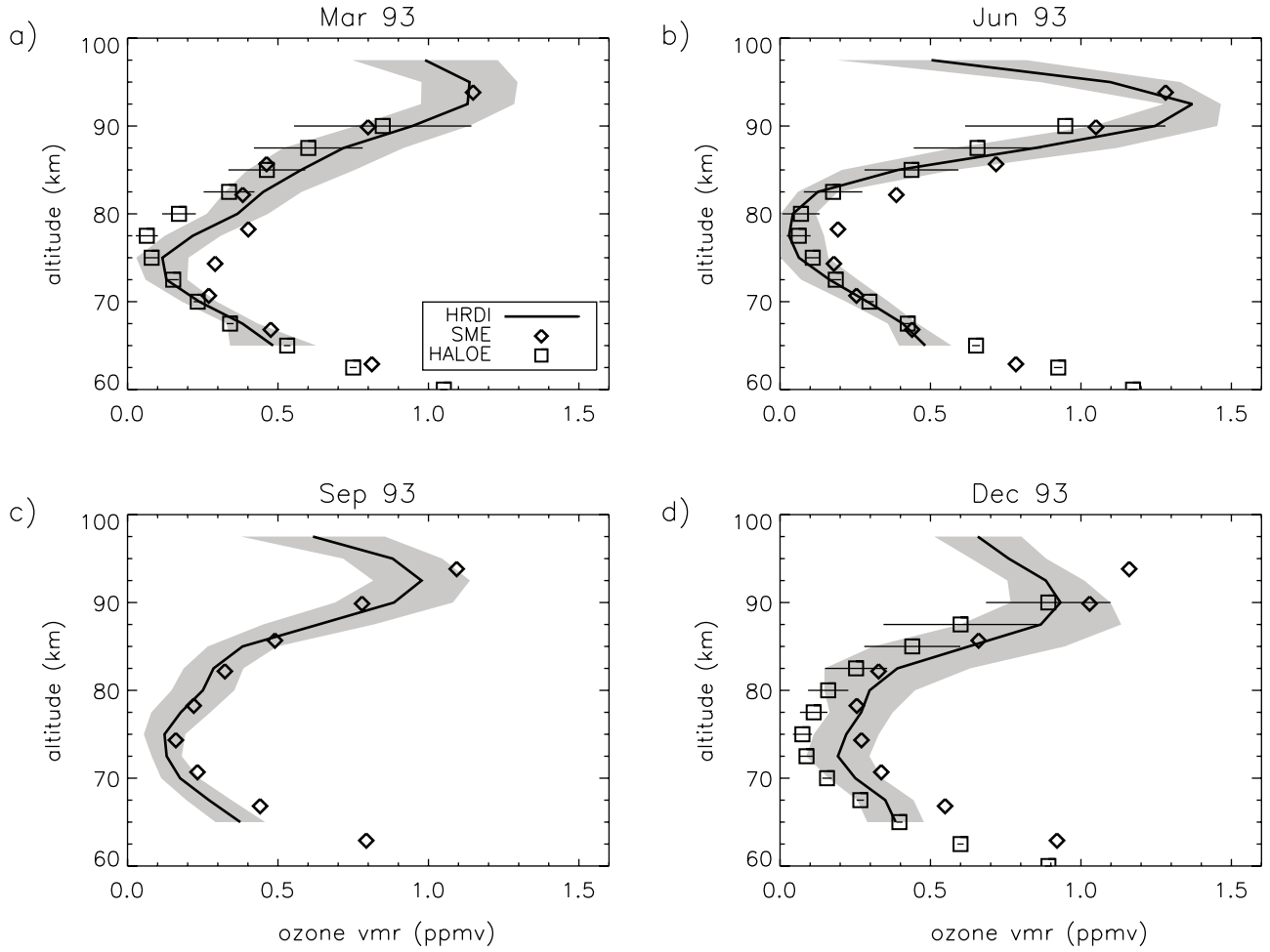


**Figure 6.** Ozone mixing ratios at 45°N measured by HRDI during 1993 (solid line) compared with data from the SME climatology. The shaded regions represents the standard deviation (±1σ) of HRDI observations taken within 30 min of 1500 LT. Also shown are averages of version 19 HALOE sunset data where available (error bars ±1σ).

system, an empirical approach has been adopted to correct for drifts in sensitivity. For each emission line, the line of sight brightnesses at each tangent height are fit with a linear trend. Next, these trends are averaged to determine a trend for each emission line. These average trends are then used to correct brightnesses at all altitudes. This approach avoids introducing any altitude dependence on the correction and is reasonable since the instrument sensitivity should be independent of viewing tangent height. An evaluation of instrument sensitivity trends is presented in [*Skinner et al.*, 1999]. As the accuracy of the estimation of instrument trends improves, it should extend the period over which long-term trends in ozone can be analyzed.

## 5. Validation

[22] To date, there are no published data of ozone observations that are coincident with HRDI observations. Ideally, to validate HRDI measurements, comparisons would be made of individual profiles taken at the same time and location. Unfortunately, such observations are currently unavailable, and instead comparisons with historical data sets are made, along with observations by the HALOE instrument.

[23] We first compare HRDI data with observations made between 30 April and 1 May 1985 by the ATMOS experiment [*Gunson et al.*, 1990]. Figure 5 presents data from occultation observations taken at 48°S and 28°S latitudes. The times of these observations were approximately 0700 LT and 1830 LT respectively. HRDI data are averages of all profiles within 4° latitude and are at approximately 0850 LT and 1720 LT. Sunset measurements appear to be in excellent agreement throughout the altitude range. While near 90 km sunrise measurements appear to be in good agreement, between 70 and 80 km a large discrepancy exists. ATMOS was unable to detect a measurable amount of ozone at 74 km, and placed an upper limit on the ozone mixing ratio of 0.002 ppmv. HRDI estimates are considerably higher, at around 0.1 ppmv. One possible cause of the difference is that they occur at different local times. Modeling studies show that at these altitudes, ozone concentrations plummet at sunrise, but rebound shortly afterward [*Allen et al.*, 1984]. Concentrations can triple in the two hours of local time that separate ATMOS and HRDI observations.

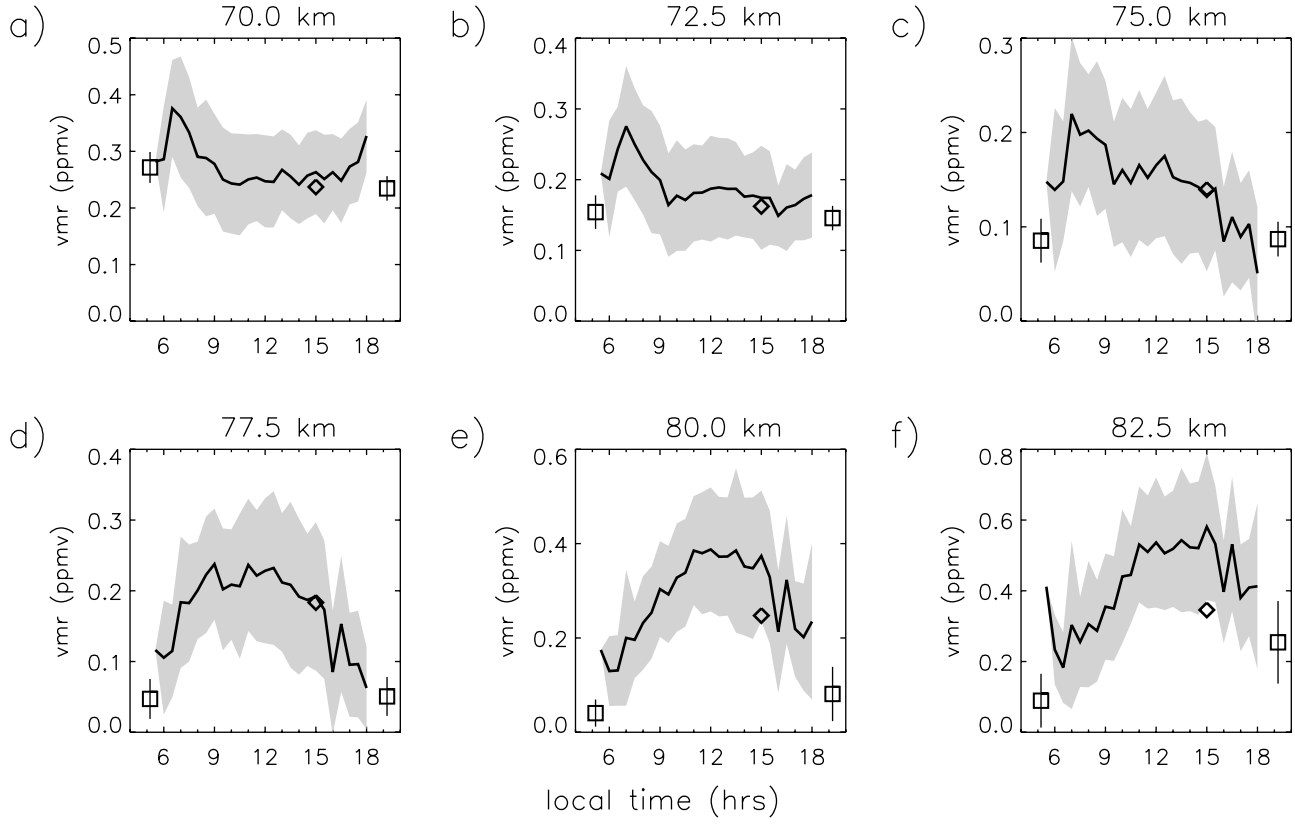


**Figure 7.** HRDI observations of the diurnal cycle in ozone at 40°N ± 5°. HRDI ozone (solid line) are average values binned every 20 min in local time, between 22 April 1994 and 22 May 1994. The shaded regions represent the standard deviation (±1σ) of HRDI observations. CIRA climatology values (diamonds) and HALOE observations (squares) are plotted for comparison.

[24] The only ozone reference model that covers the upper mesosphere is the COSPAR International Reference Atmosphere (CIRA) [*Keating et al.*, 1996]. Above 0.155 mbar (approximately 63 km) the daytime model values are based entirely on data from the SME satellite, and thus represent ozone values at approximately 1500 LT. Figure 6 presents comparisons of HRDI and SME monthly mean altitude profiles of ozone mixing ratios at 45°N. SME values are monthly mean measurements from 1982 to 1984. Random errors in SME data are reported to be approximately 10% below 80 km to 20% at 90 km. Systematic errors are estimated to be 15%, but could be as large as 50%. The solid line represents the mean of 1993 HRDI observations taken within 30 min of 1500 LT. Shaded regions are the standard deviation (±1σ) of this mean, and will include not only measurement error, but also geophysical variability that occurs around a longitude circle. Also shown are HALOE version 19 sunset data where available for the same periods [*Brühl et al.*, 1996]. In the altitude region where observations overlap, there appears to be good agreement between the data sets, with virtually all observations agreeing to within ±1σ. Those points outside this range are mostly in the altitude range 75 to 80 km, where both measurement and systematic error are at a maximum and also where there exists a substantial local time variation (see Section 6). All profiles indicate a minimum in ozone between 70 and 80 km, with rapidly increasing concentrations above 80 km. In addition, a large seasonal variation is seen in the peak value of the secondary maximum, with values in summer approximately 50% greater than in winter.

## 6. Ozone Diurnal Variations

[25] Perhaps the most interesting feature of the HRDI data set is its coverage of all daylight local times in the altitude range where there exists significant diurnal variations. On any particular day of observing, UARS orbits the Earth approximately 15 times. At a fixed latitude, observations are limited to one local time and are nearly equally spaced in longitude. Measurements at each latitude can therefore be averaged to obtain a zonal mean. The 57° orbit inclination of the UARS satellite means HRDI observations precess in local time 20 min per day, and so cover all local times every 36 days. Approximately every 36 days the satellite undergoes what is termed a "yaw maneuver" in which the spacecraft orientation is rotated 180°, so that the portion of the satellite which was pointing in the direction of satellite motion is pointing away from this direction. This is done to maintain the satellite's aspect toward the Sun for thermal and power requirements.

[26] By looking at HRDI ozone data from one satellite yaw cycle, i.e., the period between satellite yaws, good coverage in local time is obtained at a given latitude. Figure 7 show mesospheric ozone observations as a function of local time for the period between 23 April 1994 and 22 May 1994. The

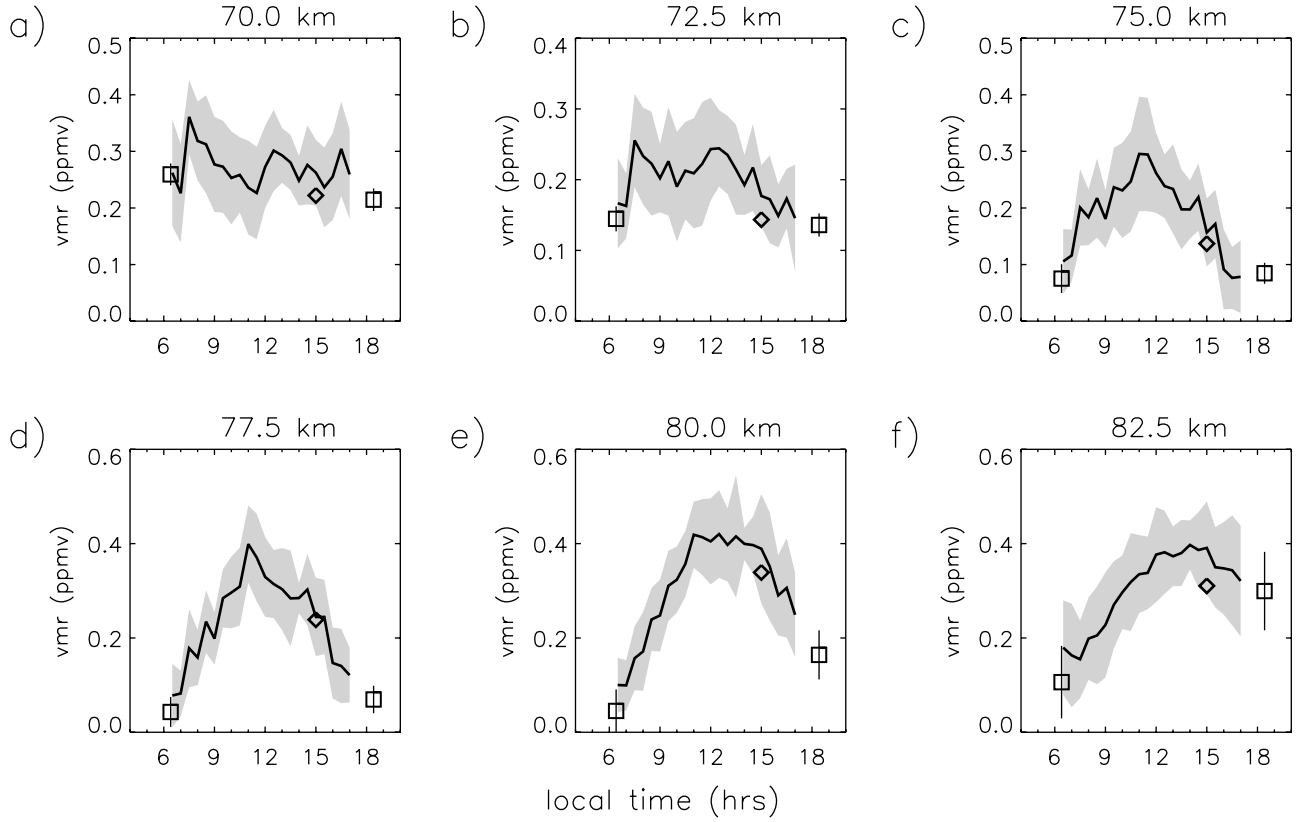


**Figure 8.** As Figure 7 but at the equator.

mean of all observations are shown that fell within 5 degrees latitude of 40°N (solid line), along with the average variance. Plotted for comparison are UARS HALOE version 19 sunrise and sunset ozone observations. In addition, values from the CIRA reference atmosphere [*Keating et al.*, 1996] are overplotted. HRDI measurements appear to be in excellent agreement with the SME based climatology. At most altitudes, HALOE observations fall within 1σ of the HRDI sample mean nearest to the HALOE observations. The HRDI data "connect" the observations of HALOE and SME, and differences between them are now seen as part of the diurnal cycle in ozone. At lower altitudes, a sharp, short-lived increase in ozone is observed shortly after sunrise. This increase has been seen in models [see, e.g., *Vaughan*, 1984] and in both satellite and ground-based observations [*Ricaud et al.*, 1996]. Variations in local time are much larger than the variations seen by ground based techniques, but this is likely due to the fact that the vertical resolution of the microwave technique would tend to smear out much of the fine vertical structure. The postsunrise increase has been attributed to an increase in molecular oxygen photolysis rates (and therefore an increase in atomic oxygen and ozone production) that is not immediately balanced by atomic oxygen destruction through reactions with the odd-hydrogen species OH and $HO_2$. Not only is the local-time behavior of ozone at 70 km similar to MLS observations during 1992, but also the absolute values are comparable (both ranging from 0.2 to 0.4 ppmv) [*Ricaud et al.*, 1996]. At higher altitudes the time which ozone reaches its daytime maximum shifts to later in the day. *Vaughan* [1984] attributes this shift to an increase in the time taken for conversion of water vapor to odd-hydrogen, and therefore a delay in ozone destruction.

[27] Diurnal variations at the equator are qualitatively the same as those at 40°N (see Figure 8). Again a brief increase is seen after sunrise at the lowest altitude and the time of maximum daytime ozone moves to later local times with increasing altitude. At 82.5 km there exists a factor of 3 difference between sunrise and sunset HALOE observations. The HRDI measurements show that this change is part of a diurnal cycle in which ozone concentrations increase throughout most of the day. While this variation is in part the result of the odd-hydrogen chemistry discussed in detail in the modeling study of *Allen et al.* [1984], there is also likely a dynamically induced component to the ozone diurnal variation. In the daytime, ozone is short-lived but can nevertheless be affected by atmospheric motions because it is in photochemical equilibrium with atomic oxygen which has a relatively long chemical lifetime (from about a day near 80 km to a week at 100 km [*Brasseur and Solomon*, 1986]). Ozone production by recombination is approximately balanced by ozone losses through photolysis:

$$\frac{\partial[O_3]}{\partial t} \simeq k_6(T)[O][O_2][M] - J_{O_3}[O_3] = 0, \qquad (17)$$

where $k_6$ is the temperature dependent 3-body recombination rate constant for ozone production, and $J_{O_3}$ is the total ozone photolysis rate. Solving for ozone,

$$[O_3] \simeq \frac{k_6(T)[O][O_2][M]}{J_{O_3}}. \qquad (18)$$

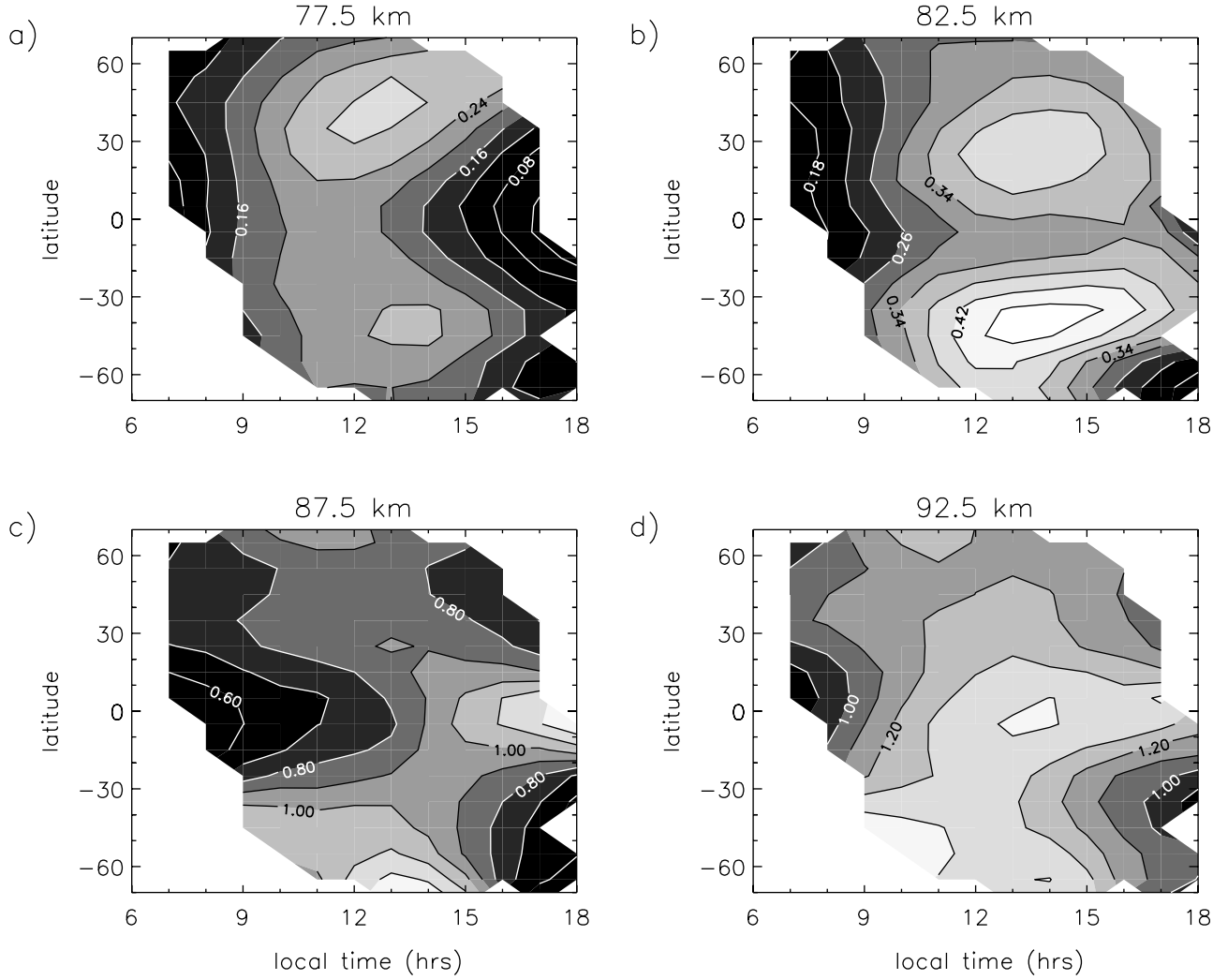


**Figure 9.** Latitude versus local time contour plots of HRDI monthly mean ozone mixing ratios (ppmv) for March 1993. Data has been smoothed with a (1, 4, 1) triangular filter.

Above 50 km the atmosphere is optically thin to radiation that photolyzes ozone and so the denominator in (18) is practically constant during the day [*Brasseur and Solomon*, 1986]. Therefore, daytime ozone will reflect the atomic oxygen concentration, the temperature and the neutral density (all changed by the presence of tides in the MLT). Studies of nightglow have shown that the solar migrating diurnal tide can significantly affect the distribution of atomic oxygen in the MLT [see, e.g., *Burrage et al.*, 1994; *Roble and Shepherd*, 1997; *Yee et al.*, 1997]. Modeled vertical winds associated with the migrating diurnal tide can exceed 10 cm $s^{-1}$ at the equator [*Hagan et al.*, 1999]. This, along with the presence of large vertical gradients in atomic oxygen mixing ratios, can lead to large (factor of 5 at 95 km) changes in atomic oxygen. Essentially, tides "pump" air rich in atomic oxygen down from the lower thermosphere to the mesosphere, where it combines with molecular oxygen to form ozone.

[28] The relative importance of vertical advection, compared to chemical and diffusive processes, in determining atomic oxygen distributions can be estimated by examining the time constants for each process. As was mentioned before, chemical lifetimes are greater than a day. Assuming a scale height ($H$) for atomic oxygen of 5 km [*Brasseur and Solomon*, 1986], the time constant for vertical advection ($\tau_w = H/w$) is approximately 14 hours. Using an eddy diffusion coefficient ($K$) of 35 $m^2/s$ [*López-Puertas et al.*, 2000] we find the time constant for diffusion ($\tau_K = H^2/K$) of around 71 hours. The time constant for molecular diffusion would be even longer because the mesopause region is below the turbopause. Given that the time constant for tidal advection appears to be the shortest, this process will likely be the dominant source of atomic oxygen variability near the equator. This is confirmed by the clear presence of tidal signatures seen in ozone mixing ratios presented in Figure 9. The latitude/local time structure of ozone observed between 77.5 and 92.5 km appears to be characteristic of the first symmetric propagating diurnal tide. At 92.5 km ozone mixing ratios peak at the equator at 1400 LT, while around 10 to 15 km lower in altitude, ozone at 1400 LT peaks at ±30° latitude. This indicates a vertical wavelength of around 20 to 30 km,

which is again consistent with the wavelength of the propagating diurnal tide.

## 7. Conclusion

[29] We shave shown that observations of the molecular oxygen Atmospheric band can be used to derive ozone concentrations in the mesosphere and lower thermosphere. Measurements based on HRDI observations show good agreement with previous satellite measurements, and with the UARS HALOE instrument. HRDI observations confirm the existence of an ozone secondary maximum around 92.5 km, and a deep minimum near 75 km. The new HRDI data set provides the first near global long term observations of ozone between 65 and 97.5 km. High temporal resolution measurements of mesospheric ozone show diurnal variations not previously observed by satellite instruments. Near the mesopause region large diurnal variability is observed, which is the result of a combination of chemical and dynamical control. Given that MLT ozone appears to be controlled in part by tidal motions, there are several implications for satellite data analysis and modeling. First, quantitative comparisons between observed and modeled ozone near the mesopause will require models that include the effects of atmospheric tides. Therefore, to establish whether there exists a model ozone deficit in this region will typically require the use of a 3-dimensional model. Second, since tidal amplitudes have been shown to vary on seasonal and annual timescales *Burrage et al.* [1995], understanding ozone variability requires knowledge of tidal variability. Last, analysis of Sun-synchronous data sets (e.g., SME ozone measurements) must take into account that they sample the tidal influence at just one time, and so do not represent a daytime or diurnal mean value.

[30] **Acknowledgments.** This work is sponsored by NASA through contract NAG 5-6709. The National Center for Atmospheric Research is operated by the University Corporation for Atmospheric Research under the sponsorship of the National Science Foundation.

## References

Ackerman, M., Ultraviolet solar radiation related to mesospheric processes, in *Mesospheric Models and Related Experiments*, edited by G. Fiocco, pp. 149–159, D. Reidel, Norwell, Mass., 1971.

Allen, M., J. I. Lunine, and Y. L. Yung, The vertical distribution of ozone in the mesosphere and lower thermosphere, *J. Geophys. Res.*, *89*, 4841–4872, 1984.

Brasseur, G., and S. Solomon, *Aeronomy of the Middle Atmosphere*, 2nd ed., 452 pp., D. Reidel, Norwell, Mass., 1986.

Brueckner, G. E., K. Edlow, L. Floyd, J. Lean, and M. VanHoosier, The Solar Ultraviolet Spectral Irradiance Monitor (SUSIM) experiment on board the Upper Atmosphere Research Satellite (UARS), *J. Geophys. Res.*, *98*, 10,695–10,711, 1993.

Brühl, C., et al., HALOE ozone channel validation, *J. Geophys. Res.*, *101*, 10,217–10,240, 1996.

Bucholtz, A., W. R. Skinner, V. J. Abreu, and P. B. Hays, The dayglow of the $O_2$ Atmospheric band system, *Planet. Space. Sci.*, *34*, 1031–1035, 1986.

Burch, D. E., and D. A. Gryvnak, Strengths, widths, and shapes of the oxygen lines near 13,100 $cm^{-1}$ (7620Å), *Appl. Opt.*, *8*, 1969.

Burrage, M. D., N. Arvin, W. R. Skinner, and P. B. Hays, Observations of the $O_2$ atmospheric band nightglow by the High Resolution Doppler Imager, *J. Geophys. Res.*, *99*, 15,017–15,023, 1994.

Burrage, M. D., M. E. Hagan, W. R. Skinner, D. L. Wu, and P. B. Hays, Long-term variability in the solar diurnal tide observed by HRDI and simulated by the GSWM, *Geophys. Res. Lett.*, *22*, 2641–2644, 1995.

Cooper, I. A., P. J. Neill, and J. R. Wiesenfeld, Relative quantum yield of $O(^1D_2)$ following ozone photolysis between 221 and 243.5 nm, *J. Geophys. Res.*, *98*, 12,795–12,800, 1993.

DeMore, W. B., S. P. Sander, D. M. Golden, R. F. Hampson, M. J. Kurylo, C. J. Howard, A. R. Ravishankara, C. E. Kolb, and M. J. Molina, Chemical kinetics and photochemical data for use in stratospheric modeling: Evaluation number 12, *JPL Publ. 97-4*, 1997.

Gibson, S. T., H. P. F. Gies, A. J. Blake, D. G. McCoy, and P. J. Rogers, Temperature dependence in the Schumann–Runge photoabsorption continuum of oxygen, *J. Quant. Spectrosc. Radiat. Transfer*, *31*, 385–393, 1983.

Goody, R. M., and Y. L. Yung, *Atmospheric Radiation—Theoretical Basis*, Oxford Univ. Press, New York, 1989.

Green, J. G., J. Shi, and J. R. Barker, Photochemical kinetics of vibrationally excited ozone produced in the 248 nm photolysis of $O_2/O_3$ mixtures, *J. Phys. Chem. A*, *104*, 6218–6226, 2000.

Grassl, H. J., W. R. Skinner, P. B. Hays, D. A. Gell, M. D. Burrage, and D. A. Ortland, Atmospheric wind measurements with the High-Resolution Doppler Imager, *J. Spacecr. Rockets*, *32*, 169–176, 1995.

Gunson, M. R., C. B. Farmer, R. H. Norton, R. Zander, C. P. Rinsland, J. H. Shaw, and B.-C. Gao, Measurements of $CH_4$, $N_2O$, CO, $H_2O$, and $O_3$ in the middle atmosphere by the Atmospheric Trace Molecule Spectroscopy Experiment on Spacelab 3, *J. Geophys. Res.*, *95*, 13,867–13,882, 1990.

Hagan, M. E., M. D. Burrage, J. M. Forbes, J. Hackney, W. J. Randel, and X. Zhang, GSWM-98: Results for migrating solar tides, *J. Geophys. Res.*, *104*, 6813–6827, 1999.

Hays, P. B., and R. G. Roble, Observation of mesospheric ozone at low latitudes, *Planet. Space Sci.*, *21*, 273–279, 1973.

Hays, P. B., V. J. Abreu, M. E. Dobbs, D. A. Gell, H. J. Grassl, and W. R. Skinner, The High-Resolution Doppler Imager on the Upper Atmosphere Research Satellite, *J. Geophys. Res.*, *98*, 10,713–10,723, 1993.

Hedin, A. E., Extension of the MSIS thermosphere into the middle and lower atmosphere, *J. Geophys. Res.*, *96*, 1159–1172, 1991.

Keating, G. M., M. C. Pitts, G. Brasseur, and A. De Rudder, Response of middle atmosphere to short-term solar ultraviolet variations, 1, Observations, *J. Geophys. Res.*, *92*, 889–902, 1987.

Keating, G. M., L. S. Chiou, and N. C. Hsu, Improved ozone reference models for the COSPAR international reference atmosphere, *Adv. Space Res.*, *18*, 11–58, 1996.

Kernahan, J. A., and P. H.-L. Pang, Experimental determination of absolute A coefficients for "forbidden" atomic oxygen lines, *Can. J. Phys.*, *53*, 455–458, 1975.

Khosravi, R., G. P. Brasseur, A. K. Smith, D. W. Rusch, and J. M. Russell III, Significant reduction in the stratospheric ozone deficit using a three-dimensional model constrained with UARS data, *J. Geophys. Res.*, *103*, 16,203–16,219, 1998.

Koppers, G. A. A., and D. P. Murtagh, Model studies of the influence of $O_2$ photodissociation parameterizations in the Schumann–Runge bands on ozone related photolysis in the upper atmosphere, *Ann. Geophys.*, *14*, 68–79, 1996.

Lacoursiere, J., S. A. Meyer, G. W. Faris, T. G. Slanger, B. R. Lewis, and S. T. Gibson, The $O(^1D)$ yield of $O_2$ photodissociation near H Lyman-$\alpha$ (121.6 nm), *J. Chem. Phys.*, *110*, 1949–1958, 1999.

Lee, L. C., and T. G. Slanger, Observations on $O(^1D \rightarrow {}^3P)$ and $O_2(b^1\Sigma_g^+ \rightarrow X^3\Sigma_g^-)$ following $O_2$ photodissociation, *J. Chem.*, *69*, 4053–4060, 1978.

López-González, M. J., J. J. López-Moreno, and R. Rodrigo, Altitude profiles of the Atmospheric system of $O_2$ and of the green line emission, *Planet. Space Sci.*, *40*, 783–795, 1992.

López-Puertas, M., M. Á. López-Valverde, R. R. Garcia, and R. G. Roble, A review of $CO_2$ and CO abundances in the middle atmosphere, in *Atmospheric Science Across the Stratopause*, *Geophys. Monogr. Ser.*, vol. 123, edited by D. E. Siskind, S. D. Eckermann, and M. E. Summers, pp. 83–100, AGU, Washington, D. C., 2000.

McDade, I. C., D. P. Murtagh, R. G. H. Greer, P. H. G. Dickinson, G. Witt, J. Stegman, E. J. Llewellyn, I. Thomas, and D. B. Jenkins, ETON 2: Quenching parameters for the proposed precursors of $O_2(b^1\Sigma_g^+)$ and $O(^1S)$ in the terrestrial nightglow, *Planet. Space Sci.*, *34*, 789–800, 1986.

Mlynczak, M. G., An evaluation of the rate of absorption of solar radiation in the $O_2(X^3\Sigma_g \rightarrow b^1\Sigma_g)$ transition, *Geophys. Res. Lett.*, *14*, 1439–1442, 1993.

Mlynczak, M. G., and D. S. Olander, On the utility of the molecular oxygen dayglow emissions as proxies for middle atmosphere ozone, *Geophys. Res. Lett.*, *22*, 1377–1380, 1995.

Mlynczak, M. G., and S. Solomon, A detailed evaluation of the heating efficiency in the middle atmosphere, *J. Geophys. Res.*, *98*, 10,517–10,541, 1993.

Mlynczak, M. G., R. R. Garcia, R. G. Roble, and M. Hagan, Solar energy deposition rates in the mesosphere derived from airglow measurements: Implications for the ozone model deficit problem, *J. Geophys. Res.*, *105*, 17,527–17,538, 2000.

Mlynczak, M. G., F. Morgan, J.-H. Yee, P. Espy, D. Murtagh, B. Marshall, and F. Schmidlin, Simultaneous measurements of the $O_2(^1\Delta)$ and $O_2(^1\Sigma)$

airglows and ozone in the daytime mesosphere, *Geophys. Res. Lett.*, *28*, 999–1002, 2001.

Molina, L. T., and M. J. Molina, Absolute absorption cross sections of ozone in the 185–350 nm wavelength range, *J. Geophys. Res.*, *91*, 14,501–14,508, 1986.

Nicholls, R. W., Franck-Condon factors to high vibrational quantum numbers V: $O_2$ band systems, *J. Res. NBS*, *69A*, 369, 1965.

Ortland, D. A., P. B. Hays, W. R. Skinner, and J.-H. Yee, Remote sensing of mesospheric temperatures and $O_2(^1\Sigma)$ band volume emission rates with the High Resolution Doppler Imager, *J. Geophys. Res.*, *103*, 1821–1835, 1998.

Reber, C. A., C. E. Trevathan, R. J. McNeal, and M. R. Luther, The Upper Atmosphere Research Satellite (UARS) mission, *J. Geophys. Res.*, *98*, 10,643–10,647, 1993.

Ricaud, P., J. de La Noe, B. J. Connor, L. Froidevaux, J. W. Waters, R. S. Harwood, I. A. MacKenzie, and G. E. Peckman, Diurnal variability of mesospheric ozone as measured by the UARS microwave limb sounder instrument: Theoretical and ground-based validations, *J. Geophys. Res.*, *101*, 10,077–10,089, 1996.

Roble, R. G., and G. G. Shepherd, An analysis of wind imaging interferometer observations of $O(^1S)$ equatorial emission rates using the thermosphere–ionosphere–mesosphere–electrodynamics general circulation model, *J. Geophys. Res.*, *102*, 2467–2474, 1997.

Rodgers, C. D., Retrieval of atmospheric temperature and composition from remote measurements of thermal radiation, *Rev. Geophys.*, *14*, 609–624, 1976.

Siskind, D. E., B. J. Connor, R. S. Eckman, E. E. Remsberg, J. J. Tsou, and A. Parrish, An intercomparison of model ozone deficits in the upper stratosphere and mesosphere from two data sets, *J. Geophys. Res.*, *100*, 11,191–11,201, 1995.

Skinner, W. R., D. A. Gell, A. R. Marshall, P. B. Hays, J. F. Kafkalidis, and D. R. Marsh, The High Resolution Doppler Imager: Instrument performance from late 1991 to mid-1999, *Proc. SPIE*, *3756*, 309–315, 1999.

Solomon, S., D. W. Rusch, R. J. Thomas, and R. S. Eckman, Comparison of mesospheric ozone abundances measured by the solar mesosphere explorer and model calculations, *Geophys. Res. Lett.*, *10*, 249–252, 1983.

Talukdar, R. K., C. A. Longfellow, M. K. Gilles, and A. R. Ravishankara, Quantum yields of $O(^1D)$ in the photolysis of ozone between 289 and 329 nm as a function of temperature, *Geophys. Res. Lett.*, *25*, 143–146, 1998.

Thomas, R. J., C. A. Barth, D. W. Rusch, and R. W. Sanders, Solar Mesospheric Explorer Near-Infrared Spectrometer: Measurements of 1.27-μm radiances and the inference of mesospheric ozone, *J. Geophys. Res.*, *89*, 9569–9580, 1984.

Vaughan, G., Mesospheric ozone—Theory and observation, *Q. J. R. Meteorol. Soc.*, *110*, 239–260, 1984.

Wallace, L., and D. M. Hunten, Dayglow of the Oxygen A Band, *J. Geophys. Res.*, *73*, 4813–4834, 1968.

Yee, J. H., G. Crowely, R. G. Roble, W. R. Skinner, M. D. Burrage, and P. B. Hays, Global simulations and observations of $O(^1S)$, $O_2(^1\Sigma)$, and OH mesospheric nightglow emissions, *J. Geophys. Res.*, *102*, 19,949–19,968, 1997.

Yoshino, K., A. S.-C. Cheung, J. R. Esmond, W. H. Parkinson, D. E. Freeman, S. L. Guberman, A. Jenouvrier, B. Coquart, and M. F. Merienne, Improved absorption cross-sections of oxygen in the wavelength region 205–240 nm of the Herzberg Continuum, *Planet. Space Sci.*, *36*, 1469–1475, 1988.

Yoshino, K., J. R. Esmond, D. E. Freeman, and W. H. Parkinson, Measurements of absolute absorption cross sections of ozone in the 185- to 254-nm wavelength region and the temperature dependence, *J. Geophys. Res.*, *98*, 5205–5211, 1993.

P. B. Hays, A. R. Marshall, and W. R. Skinner, Department of Atmospheric, Oceanic, and Space Science, University of Michigan, Ann Arbor, MI, USA.

D. R. Marsh, High Altitude Observatory, National Center for Atmospheric Research, P.O. Box 3000, Boulder, CO 80307-3000, USA. (marsh@ucar.edu)

D. A. Ortland, Northwest Research Associates, Seattle, WA, USA.

J.-H. Yee, Applied Physics Laboratory, Johns Hopkins University, Laurel, MD, USA.